Case Studies in Thermal Engineering 78 (2026) 107624

Contents lists available at ScienceDirect

Case Studies in Thermal Engineering

journal homepage: www.elsevier.com/locate/csite

Triangular-shell finned latent heat storage: Orientation and fin-design effects

Fathi Alimi [a], Nashmi H. Alrasheedi [b], Mohammad Hossein Heidarshenas [c], Mohamed Bouzidi [d], Mansour Mohamed [d], Khalil Hajlaoui [b], Xusheng Hu [e], Mehdi Ghalambaz [f,g,*]

[a] Department of Chemistry, College of Science, University of Ha'il, P.O. Box 2440, Ha'il, 81441, Saudi Arabia
[b] College of Engineering, Imam Mohammad Ibn Saud Islamic University (IMSIU), Riyadh, Kingdom of Saudi Arabia
[c] Department of Mechanical and Nuclear Engineering, Kansas State University, Manhattan, KS, USA
[d] Department of Physics, College of Science, University of Ha'il, P.O. Box 2440, Ha'il, Saudi Arabia
[e] College of Mechanical and Electrical Engineering, Harbin Engineering University, Harbin, 150001, China
[f] Department of Mathematical Sciences, Saveetha School of Engineering, SIMATS, Chennai, India
[g] Refrigeration and Air Conditioning Technical Engineering Department, College of Technical Engineering, The Islamic University, Najaf, Iraq

GRAPHICAL ABSTRACT

The finned double pipe LHS in a triangular shell for (a) upward and (b) downward orientation.

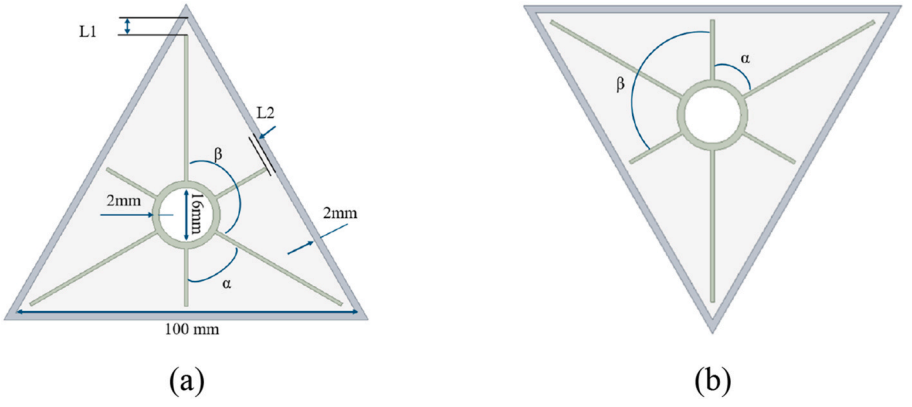

* Corresponding author. Department of Mathematical Sciences, Saveetha School of Engineering, SIMATS, Chennai, India
E-mail addresses: f.alimi@uoh.edu.sa (F. Alimi), nhrasheedi@imamu.edu.sa (N.H. Alrasheedi), Heidarshenas@ksu.edu (M.H. Heidarshenas), elbouzidimed16@yahoo.com (M. Bouzidi), mansour.m@uoh.edu.sa (M. Mohamed), kmhajlaoui@imamu.edu.sa (K. Hajlaoui), xusheng.hu@hrbeu.edu.cn (X. Hu), ghalambaz.mehdi@gmail.com (M. Ghalambaz).

https://doi.org/10.1016/j.csite.2025.107624
Received 16 September 2025; Received in revised form 18 December 2025; Accepted 27 December 2025
Available online 29 December 2025

A R T I C L E I N F O

Keywords:
Phase change materials (PCM)
Triangular-shell latent heat storage
Finned double pipe heat exchanger
Fin geometry optimization

A B S T R A C T

This study investigates the melting behavior of a finned double-pipe latent heat thermal storage (LHTES) unit enclosed in a compact triangular shell, a geometry increasingly used in modular thermal storage assemblies where space efficiency and structural rigidity are required. A fixed-temperature inner tube, uniform material set, and two gravity orientations (upward and downward) are considered to quantify how fin number and circumferential fin arrangement influence heat-storage performance. A validated enthalpy-porosity model is used to simulate the coupled conduction–convection melting process. Results show that increasing the fin count from three to six substantially enhances circumferential heat spreading, raising the average charging rate by 42 % and shortening the melting time by 29.5 %. Among the downward configurations, the six-fin case (Case 4) exhibits the strongest overall melting performance among the downward configurations. A non-uniform fin layout in the upward orientation (Case 9) yields the highest overall performance. When the optimal cases are compared, the upward configuration achieves only a modest improvement in both storage rate (6.5 %) and melting time (7.5 %) relative to the best downward case, indicating that the selected fin architecture significantly mitigates gravity-induced orientation sensitivity. The novelty of this work lies in combining a triangular shell, non-uniform circumferential fin distributions, and dual orientations within a unified numerical framework to identify robust fin arrangements for compact LHTES units. The findings demonstrate that appropriately designed fins can reduce the performance penalty typically associated with unfavorable gravitational alignment, improving applicability in installations where orientation cannot be optimized.

The following symbols are used throughout the manuscript. Units are provided for dimensional quantities.

Symbol	Description	Unit
α	Angular spacing between a long fin and an adjacent short fin	^{o}C
β	Angular spacing between two short fins	^{o}C
L_1, L_2	Fin geometric lengths	m
g	Gravitational acceleration	$m.s^{-2}$
H	Enthalpy	$J.kg^{-1}$
k	Thermal conductivity	$W.m^{-1}.K^{-1}$
L_f	Latent heat of fusion	$J.kg^{-1}$
β_T	Thermal expansion coefficient	K^{-1}
λ	Liquid fraction	1
μ	Dynamic viscosity	Pa.s
P	Pressure	Pa
C_p	Specific heat	J/kg·K
A_m	Mushy zone Darcy coefficient	–
ρ	Density of PCM	$kg.m^{-3}$
T	Temperature	K
t	Time	s
t_m	Total melting time	s
V	PCM volume	m^3
$\vec{V}$	Velocity vector	$m.s^{-1}$
E	PCM internal energy	J
S_m	Momentum source	$W.m^{-3}$
S_L	Latent heat source term	$W.m^{-3}$
Subscripts		
eff	Effective value	
ref	Reference	
i	Initial	
e	Equilibrium	
m	Momentum	
L	Latent heat	
Acronyms		
PCM	Phase Change Material	
HTF	Heat Transfer Fluid	
LHS	Latent Heat Storage	
LHTES	Latent Heat Thermal Energy Storage	

1. Introduction

The thermal behavior of latent heat storage systems is governed not only by PCM properties but also by the geometry that confines them, which strongly influences melting dynamics by altering conduction pathways and buoyancy-driven circulation. Comparative

studies across rectangular, triangular, and cylindrical domains show that noncircular or constrained cavities, particularly triangular enclosures, generate asymmetric melting fronts and orientation-dependent convection structures [1,2]. Recent numerical and experimental investigations further demonstrate that variations in shell configuration, such as inclined arrangements, wavy or undulated PCM containers, and embedded elliptic tubes, can significantly modify natural-convection patterns and the progression of the melt front [3–8]. These effects highlight that enclosure-driven flow behavior must be accounted for when designing compact LHTES units, especially when asymmetric geometries such as triangular shells are used [9–11].

Beyond enclosure geometry, extensive research has focused on improving the effective thermal conductivity of PCMs through nano-enhancement, porous media, and hybrid thermal management strategies. Nano-encapsulated and nano-enhanced PCMs (NEPCM) have shown substantial improvements in melting rate and heat transport efficiency, both in thermal storage units and in finned heat pipe configurations where nanoparticles intensify conduction and stabilize the melt front [12–14]. These studies collectively show that conductivity enhancement remains one of the dominant strategies for accelerating phase transition in LHTES. Broader reviews of nanofluid and PCM-based thermal management systems similarly highlight that nanoparticle dispersion, encapsulation techniques, and hybrid NEPCM formulations can markedly increase thermal responsiveness in applications ranging from heat pipes to battery cooling [14,15]. Experimental and numerical investigations further demonstrate that combining PCMs with high conductivity features, such as metal foams, branched or tree-shaped fins, and fin PCM composite structures, provides additional pathways for enhancing thermal conduction and accelerating phase transition [16–18]. Studies employing NEPCM within structured porous media or along heated surfaces also confirm gains in convective and conductive heat transfer due to nanoparticle induced property augmentation [19,20]. Hybrid cooling approaches that integrate PCMs with active liquid cooling loops offer yet another class of conductivity enhancement methods, enabling improved temperature uniformity and faster heat extraction under high thermal loads [21].

Fin-based enhancement is one of the most effective methods for improving heat transfer in PCM systems, and numerous fin geometries have been proposed to accelerate melting. Radial fins with circumferential perforations have been optimized to reduce thermal resistance and promote faster heat spreading [22], while fin-metal-foam composites in compact enclosures such as honeycomb structures further improve conduction pathways and melt uniformity [23]. Several studies show that modified fin shapes, including Y-fins, wavy fins, and arch-shaped fins, can significantly intensify circumferential heat penetration in shell-and-tube and triplex-tube units [24–26]. Recent work has also explored AI-guided optimization of three-dimensional fin designs, such as sine-shaped fins, to maximize thermal response under constrained geometries [27].

A parallel line of research focuses on rapid-charging strategies, where geometric optimization, interface control, and close-contact melting are applied to shorten thermal response times. Recent reviews emphasize the role of enhanced conduction paths, optimized geometries, and interface control in accelerating phase change processes [28]. Close-contact melting approaches further reduce thermal resistance and enable significantly faster charging under constrained configurations [29]. Numerical studies also show that circumferential fin arrangements can meaningfully decrease both charging and discharging times by improving circumferential heat spreading within the PCM [30].

Although HTF tube shape and fin topology have been examined previously, the analysis in Ref. [31] remains limited to conventional shell geometries and uniformly spaced fin layouts. That study does not consider triangular enclosures or how non-uniform circumferential spacing interacts with geometric asymmetry to modify natural convection. Moreover, orientation effects were evaluated only for a single gravitational direction. The present study addresses this gap by jointly examining triangular shells, non-uniform fin spacing, and dual upward/downward orientations within a unified numerical framework.

Triangular and other polygonal casings are increasingly used in compact LHTES modules, such as in heat-pump reservoirs, solar water-heating cartridges, and industrial waste-heat recovery, because they provide higher packing density when multiple units are arranged within rectangular housings [32–34]. Compared with circular shells, a triangular casing utilizes space more efficiently within rectangular housings, reduces unused void regions, and provides inherent structural rigidity advantageous for modular assembly [35–37]. Despite these advantages, melting behavior and fin-assisted heat transfer in triangular shells remain understudied relative to circular or square geometries. This work therefore examines how fin number, fin arrangement, and gravitational orientation jointly

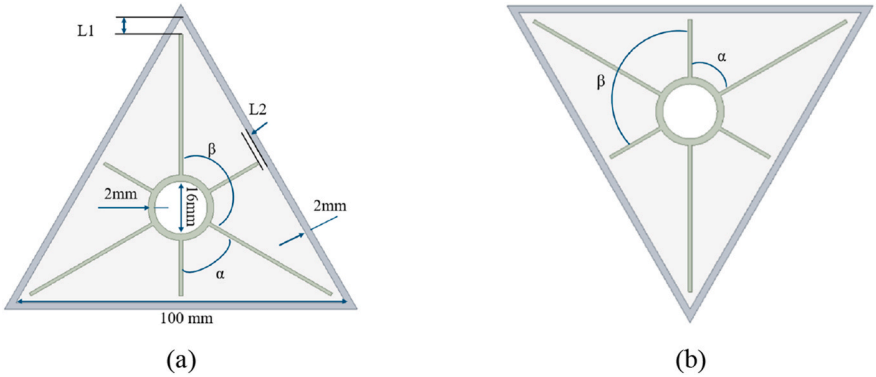

Fig. 1. Schematic of the finned double pipe LHS in a triangular shell for (a) upward and (b) downward orientation.

influence melting in a triangular-shell double-pipe system. These gaps motivate the present numerical study, which systematically evaluates the combined effects of fin count, fin geometry, circumferential fin spacing, and gravitational orientation in a triangular-shell double-pipe LHTES unit.

2. Methodology

2.1. Problem description

In this study, a finned double pipe LHS unit enclosed by an insulated triangular shell is considered (Fig. 1). The inner pipe carries the HTF and is maintained at a constant wall temperature, while the surrounding annulus is filled with a PCM initially at a uniform temperature below its melting point. The outer shell is treated as adiabatic. Gravity is included to capture buoyancy effects during melting. Two shell orientations are examined: the downward configuration (case b) and the upward configuration (case a), defined by the direction of the shell apex relative to gravity.

Geometric features consist of an inner circular tube outfitted with circumferential fins that extend radially into the PCM domain. A baseline uniform circumferential distribution of fins is established and then modified through the number of fins, the fin dimensions (length and/or thickness) for the baseline fin count, and non-uniform circumferential spacing patterns. All cases share the same material properties, inlet/thermal boundary conditions, and initial PCM temperature; only the fin architecture and/or orientation are varied according to Table 1. This design isolates the influence of fin number, fin geometry, and spacing on the charging process in each orientation while holding the thermophysical setting fixed.

The computational domain includes the inner HTF tube and the triangular shell, with the finned region fully embedded in the PCM. The constant temperature boundary condition on the inner pipe wall drives the phase change, whereas the insulated outer boundary preserves stored energy within the shell. The two orientations are analyzed under identical operating conditions so that performance differences arise solely from geometry/orientation effects. Fig. 1 provides the geometric layout and nomenclature; and the two orientations used throughout the study. The complete set of simulated cases and their distinguishing geometric attributes are summarized in Table 1.

The angular parameters α and β are defined in this study only for the six-fin configurations, where non-uniform circumferential spacing is explicitly introduced. For Cases 1–3, although long and short fins exist, these cases do not employ α and β as geometric variables, and the angles are therefore not listed in Table 1 and are shown as "–". For clarity, the actual angular spacings used in these cases are: Case 1; three long fins spaced 120° apart; Case 2; three short fins spaced 120° and long–short spacing of 60°; Case 3; long fins spaced 120° and long–short spacing of 60°. These values are fixed by the chosen geometry and are reported here for completeness.

The thermophysical parameters adopted in this work are summarized in Table 2. Copper is selected as the structural material owing to its high thermal conductivity and reliable thermal performance, which support stable heat transfer during charging. The PCM is RT35, a paraffin-based PCM widely used in low temperature thermal energy storage systems due to its suitable melting temperature, high latent heat capacity, and thermal stability. Temperature-dependent properties are assigned to the PCM in both phases, while copper is modeled with constant properties. These material specifications provide the necessary physical basis for evaluating the melting behavior under the geometric and thermal conditions considered in the present study.

Table 1
Case set and geometric variations used in this study (all other parameters identical across cases).

Case number	Number of fins	Direction	L1	L2	α	β
1	3	Downward	5	2	-	-
2	4	Downward	5	2	-	-
3	5	Downward	5	2	-	-
4	6	Downward	5	2	60	120
5	6	Downward	10	4	60	120
6	6	Downward	15	6	60	120
7	6	Downward	5	2	45	105
8	6	Downward	2	2	30	90
9	6	Upward	5	2	60	120
10	6	Upward	5	2	45	105
11	6	Upward	2	2	30	90

Table 2
Thermophysical properties of the materials used in the numerical model.

Property	Copper	PCM (RT35)	Unit
Mean density (ρ)	8978	815	kg/m^3
Specific heat (C_p)	381	2000	J/kg·K
Thermal conductivity (k)	387.6	0.2	W/m·K
Latent heat of fusion (L_f)	–	160000	J/kg
Thermal expansion coefficient (β_T)	–	0.0006	1/K
Dynamic viscosity (μ)	–	0.023	Pa.s
Melting temperature range	–	32–38	°C

2.2. Mathematical modelling

The phase change process was modeled using the enthalpy-porosity formulation of Brent et al. [38,39]. In this method, each control cell within the computational domain is assigned a uniform porosity equal to the local liquid fraction. Density variations of the PCM were retained, and buoyancy effects were incorporated via the Boussinesq approximation. Laminar flow, incompressible, periodic, and Newtonian fluid assumptions were applied to the fluid flow. The system was assumed to be well insulated, so viscous dissipation and thermal losses to the surroundings were neglected [40,41]. Under these assumptions, the governing conservation equations for continuity, momentum, and energy follow the standard forms reported in Ref. [42] and are presented in Eqs. (1)–(3).

$$\nabla.\rho\vec{V}=0 \tag{1}$$

$$\rho\frac{\partial\vec{V}}{\partial t}+\rho\left(\vec{V}.\nabla\right)\vec{V}=-\nabla P+\mu\left(\nabla^2\vec{V}\right)-\rho\beta_T\left(T-T_{ref}\right)-\vec{S}_m \tag{2}$$

$$\rho C_p\frac{\partial T}{\partial t}+\nabla\left(\rho C_p\vec{V}T\right)=\nabla(k\nabla T)-S_L \tag{3}$$

Here, ρ is the PCM density (kg/m^3), u the velocity vector (m/s), μ the dynamic viscosity (Pa·s), g the gravitational acceleration (m/s^2), β_T the thermal expansion coefficient (1/K), T the temperature (K), T_{ref} is reference temperature (298K), k the thermal conductivity (W/m·K), and C_p the specific heat (J/kg·K).

The effect of phase change on the flow is represented by the momentum source term $\vec{S}_m$ in Eq. (4), which imposes a Darcy-type damping within the mushy region and models the momentum loss associated with melting/solidification. In the energy equation, the source term S_L in Eq. (5) accounts for latent-heat absorption/release during the phase transition and its influence on the temperature field, and $\vec{S}_m$ denotes the Darcy-based mushy zone momentum term (kg/m^3·s), modelling resistance to flow in partially melted PCM. This treatment is consistent with the enthalpy–porosity framework, wherein phase change enters as a Darcy-like resistance in the momentum balance and a latent-heat source in the energy balance [43].

$$\vec{S}_m=A_m\frac{(1-\lambda)^2}{\lambda^3+0.001}\vec{V} \tag{4}$$

$$S_L=\rho L_f\frac{\partial\lambda}{\partial t}+\rho L_f\nabla\left(\vec{V}\lambda\right) \tag{5}$$

Consistent with prior studies, a mushy zone constant of $A_m = 10^5$ was used for the Darcy damping term [44–46]. The damping coefficient depends on the PCM liquid fraction λ, which varies from 0 (solid) to 1 (liquid) as defined in Eq. (6) [47]. In addition, t_m denotes the total charging duration (s), while E_i and E_e represent the PCM internal energies (J) at the start and end of the melting process, respectively. The overall energy-storage rate is then calculated using Eq. (7). $\dot{E}_T$ denotes the overall energy input rate, combining sensible heat $(MC_p dT)$ and latent heat (ML_f).

$$\lambda=\frac{\Delta H}{L_f}=\left\{\begin{array}{c}0\ if\ T<T_{Solidus}\\ 1\ if\ T>T_{Liquidus}\\ \dfrac{T-T_{Solidus}}{T_{Liquidus}-T_{Solidus}}\ if\ T_{Solidus}<T<T_{Liquidus}\end{array}\right\} \tag{6}$$

$$\dot{E}_T=\frac{E_e-E_i}{t_m} \tag{7}$$

Equation (7) represents the instantaneous melting (heat storage) rate, i.e., the total latent-plus-sensible energy absorbed per unit time, expressed in watts. The average melting/storage rate reported in the results is obtained by dividing the total absorbed energy by the total melting duration.

3. Numerical modelling, grid independence and validation

3.1. Numerical modelling

The governing equations for heat transfer and melting were solved in ANSYS Fluent. Pressure velocity coupling was handled with the SIMPLE algorithm, and field gradients were evaluated using the Green-Gauss cell-based method. The QUICK scheme was applied to discretize the momentum and energy equations, while pressure corrections were computed with PRESTO. Convergence tolerances were set to 10^{-4} for continuity and momentum and 10^{-6} for energy.

A mesh-independence study was performed for the inline, uniformly finned configuration using nominal cell sizes of 1.5, 1.0, 0.5, 0.25, and 0.10 mm. Convergence was assessed with integral metrics (charging time and average heat storage rate) and with qualitative checks of liquid fraction fields. Results indicated that solutions at 0.25 mm and 0.10 mm were indistinguishable within the reporting precision, while coarser meshes ($\geq$0.5 mm) exhibited small but visible deviations in early-stage gradients near the tube and fin roots. On this basis, a 0.25 mm mesh was adopted as an accuracy cost compromise (Fig. 2). Representative liquid fraction contours at a fixed charging time for all mesh sizes are provided in Fig. 3, confirming that interface topology and thermal boundary layer structure do not change materially once the cell size is $\leq$ 0.25 mm.

A companion time-step sensitivity analysis was conducted with $\Delta t = 0.4$, 0.2, and 0.1 s under the 0.25 mm mesh. Comparisons of liquid fraction evolution showed no discernible differences between $\Delta t = 0.2$ s and $\Delta t = 0.1$ s, indicating that temporal truncation errors are negligible at $\Delta t = 0.2$ s for the present flow and thermal time scales. Consequently, $\Delta t = 0.2$ s was selected for all subsequent simulations (Fig. 2). The overlays in Fig. 4 illustrate the time-step independence, while Fig. 5 documents the mesh layout used for production runs.

Fig. 5 shows the mesh generated for the computational domain. Based on the mesh-independence study presented in Fig. 3, an element size of 0.25 mm was selected for the entire PCM region. This uniform resolution mesh provides sufficient accuracy while keeping the computational cost manageable. Additional local refinement was applied at the inner-tube wall, fin interfaces, and triangular shell boundaries to adequately resolve steep temperature gradients. The adopted mesh was confirmed to yield mesh-independent predictions of liquid-fraction evolution.

In the present configuration, melting occurs under a constrained melting regime. The PCM is encapsulated in a rigid metallic enclosure, and the solid phase remains fixed in space while only the liquid phase is allowed to flow. This assumption is widely used for PCMs housed in closed-shell LHTES units, where no relative motion or settling of the solid can occur during melting [48,49]. Close-contact melting, by contrast, involves displacement of the solid PCM due to buoyancy, gravity, or elastic loading, as observed in elastic-driven thermal buffers and free-moving solid blocks. Since the present system involves a geometrically constrained PCM and no mechanisms capable of inducing solid motion, the constrained melting model is most physically appropriate. Under this regime, momentum terms in the mushy region suppress velocity in solid and semi-solid zones, while natural convection develops only in the liquid fraction.

3.2. Validation

Model validation was carried out against the benchmark experiments of Mat et al. [44] on a horizontal triplex-tube LHS with paraffin RT82 and straight longitudinal fins welded to both the inner and middle tubes (four fins per tube; fin pitch 42 mm, fin length 480 mm, thickness 1 mm) over a 500 mm test section. The hot-water loop was maintained at 90 °C (mass flow 8.3 L min^{-1}), while the

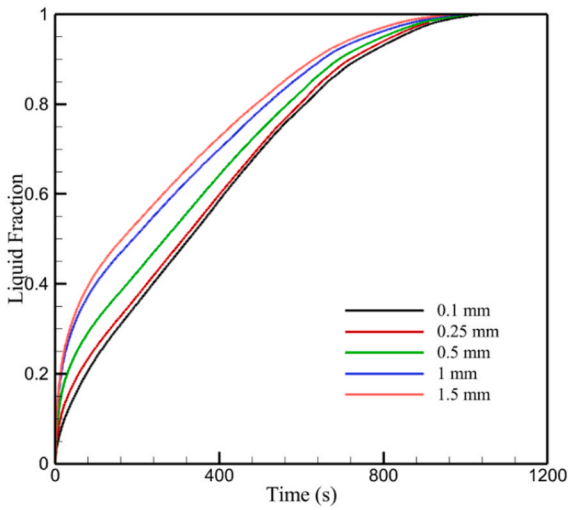

Fig. 2. Grid independence: effect of cell size (1.5–0.10 mm) on liquid fraction; selected settings: 0.25 mm, $\Delta t = 0.2$ s.

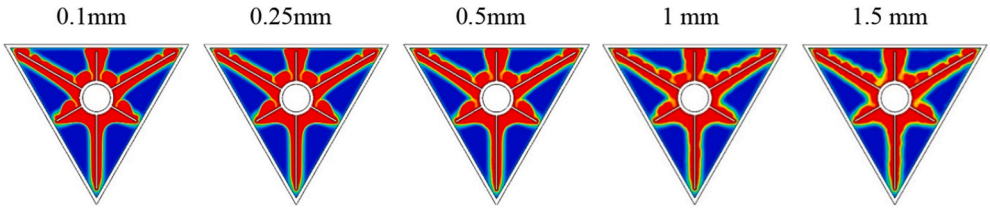

Fig. 3. liquid fraction contours at a representative charging time for each mesh size (1.5, 1.0, 0.5, 0.25, and 0.10 mm).

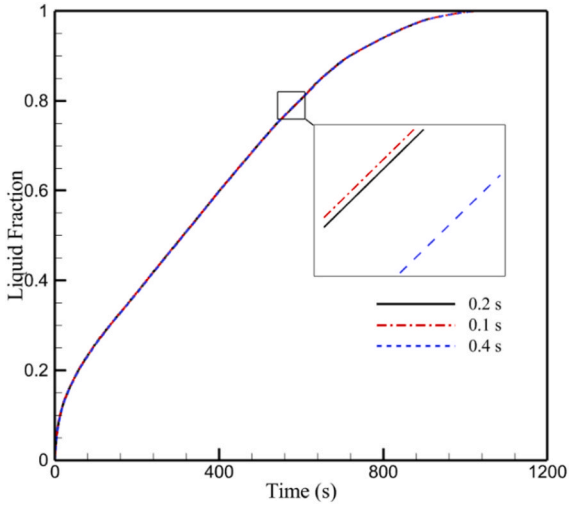

Fig. 4. Time-step sensitivity (Δt = 0.4, 0.2, 0.1 s): comparison of liquid fraction, selected settings: 0.25 mm, Δt = 0.2 s.

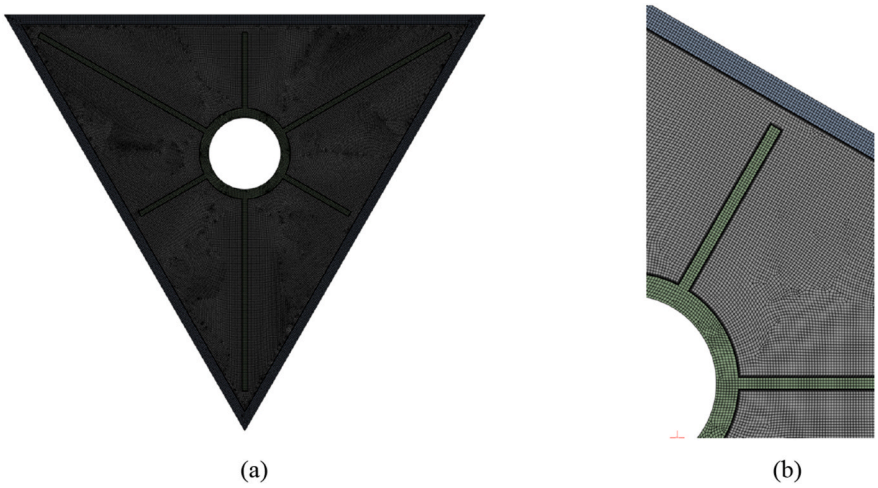

Fig. 5. (a) Computational mesh for the selected settings (0.25 mm cell size; Δt = 0.2 s): (b) detail near the inner tube and fins.

PCM initially averaged 27 °C; fifteen K-type thermocouples located 100 mm downstream sampled the PCM temperature, and the assembly was wrapped with 70 mm glass-wool insulation. Under these boundary conditions, the present model reproduced the reported average PCM temperature. Fig. 6 presents the comparison between our results and the benchmark data reported by Mat et al. [44]. The close agreement confirms the fidelity of the present enthalpy–porosity implementation.

In the absence of in-house measurements for the triangular-shell configuration, the present numerical framework was validated against the benchmark PCM melting experiment of Mat et al. [44], which considers a finned double pipe LHS unit under comparable thermal boundary conditions. Although the external geometry in Mat et al. is not triangular, the PCM properties, heating mode, and enthalpy–porosity formulation are closely related to those used in this study. To provide a time-resolved check on the model accuracy,

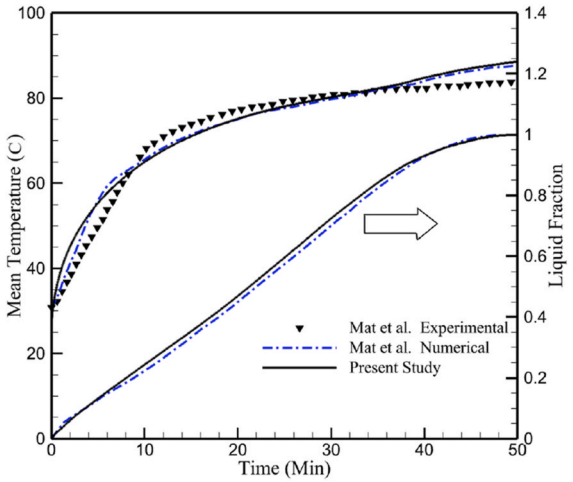

Fig. 6. (Left axis) Mean temperature and (right axis) liquid fraction versus time, present simulation compared with Mat et al. [44] for a triplex-tube LHS with straight fins.

temperatures at 300, 600, and 900 s were extracted from the present simulation and compared with interpolated experimental and numerical values reported by Mat et al. (Table 3). The mean absolute error between the present model and the experimental data is 3.69 °C (≈6.3 %), while the mean deviation from the numerical results of Mat et al. is below 1 %. This level of agreement is consistent with previous enthalpy–porosity validations for PCM systems and gives confidence that the present implementation can reliably predict the transient melting behavior in compact enclosures. The subsequent results for the triangular-shell configuration should therefore be interpreted as numerically validated predictions, pending future dedicated experiments on that specific geometry.

4. Results and discussion

4.1. Effect of fin numbers

Fig. 7 shows the melt front topology at representative charging times (e.g., 300, 600, and 900 s). With three fins (Case 1), melting initiates at the fin roots but substantial unmelted sectors persist between adjacent fins at all snapshots. The four-fin layout (Case 2) exhibits broader unmelted sectors and slower circumferential coalescence than Case 1. The five-fin configuration (Case 3) advances the interface more uniformly, with narrower residual solid regions between fins by 600 s. The six-fin configuration (Case 4) presents the most circumferentially continuous front and the smallest residual solid near inter fin mid-gaps by 900 s. This visual ranking is consistent with the time histories reported below.

Fig. 8 confirms the ordering inferred from the contours. The liquid fraction curves separate early and remain distinct over the charging window. Case 4 reaches intermediate melt levels (e.g., 0.5 and 0.75) earlier than the other cases, followed by Case 3. Case 1 progresses more gradually, while Case 2 remains lowest over the entire interval. The differences in curve slope reflect variations in the pace of melt front propagation; a detailed quantitative evaluation of the melting (heat storage) rate is presented separately later in this section to maintain a clear distinction between cumulative melt progression and instantaneous thermal performance.

Fig. 9 shows that isotherms are denser and more evenly distributed around the circumference for the six-fin case, indicating stronger and more uniform heat penetration into the PCM. The five-fin case displays similar features but with slightly thicker near wall thermal gradients. The three-fin case retains cooler bands centered between fins at intermediate times. The four-fin case exhibits the least uniform temperature field among the set. These thermal patterns corroborate the interface positions in Fig. 7 and the relative progression of liquid fraction shown in Fig. 8.

Fig. 10 provides additional evidence of how fin number modifies natural convection during melting. In Case 1, a strong pair of upward-driven recirculation cells forms along the inclined walls, with high-velocity plumes rising from the heated inner tube. Introducing a fourth fin (Case 2) disrupts this pattern by bisecting the available flow channels, producing weaker and more fragmented

Table 3
Comparison of the present numerical predictions with numerical and experimental data reported by Ref. [44] at selected time points during melting, including absolute and relative errors.

Time (s)	Present Study (°C)	[44] Numerical (°C)	[44] Experiment (°C)	Error vs [44] Numerical (°C/%)	Error vs [44] Experimental (°C/%)
300	55.34	56.00	49.74	0.66 (1.18 %)	5.60 (11.26 %)
600	64.98	65.60	67.61	0.62 (0.95 %)	2.63 (3.89 %)
900	71.00	71.42	73.84	0.42 (0.59 %)	2.84 (3.85 %)
Mean Error	–	–	–	0.57 (0.91 %)	3.69 (6.33 %)

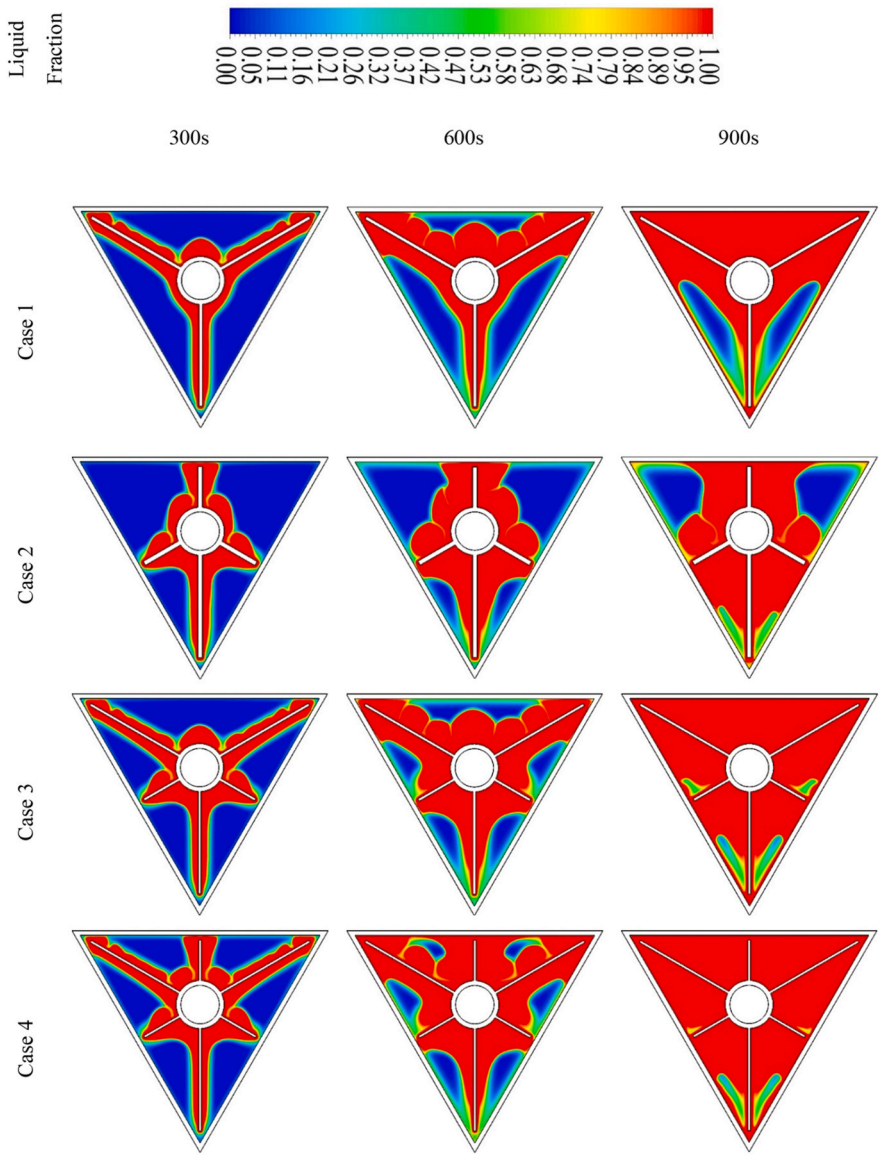

Fig. 7. Liquid fraction contours at representative charging times for Cases 1–4 to capture the fin numbers effect.

circulation zones. This constrained motion directly corresponds to the slower melting observed earlier, confirming that the added fin locally impedes convection. In Case 3, the expanded circumferential coverage allows convection cells to reorganize into a more continuous pattern, while Case 4 shows the most uniformly distributed but somewhat confined velocity field. Although convection is present in all cases, the contours demonstrate that fin placement and spacing strongly influence the strength and coherence of buoyancy-driven circulation, which in turn governs melting uniformity and rate.

Fig. 11 quantifies the effect of fin number on the average heat storage rate, which represents the overall rate of energy absorption during melting. From three to six fins (Case 1 to Case 4), the average storage rate increases from about 441 W to about 626 W (42 %), while the total melting time decreases from about 1465 s to about 1033 s (29.5 %). The five-fin case (Case 3) already delivers 35.7 % higher average rate and 27.2 % shorter time than the three-fin configuration. The increment from five to six fins yields an additional 4.5 % in rate and 3.2 % reduction in time, indicating diminishing returns beyond five fins. The four-fin case (Case 2) underperforms the three-fin baseline (rate −9.4 %, time 8.1 %) due to its unfavorable circumferential spacing. Collectively, these results identify the six-fin configuration (Case 4) as the most effective among Cases 1–4 in terms of overall thermal performance.

Although Case 2 contains more fins than Case 1, its 90° spacing interacts unfavorably with the triangular shell. The additional fin produces a narrow sector that cannot sustain buoyancy-driven recirculation, creating a conduction-limited region. In contrast, Case 1's 120° spacing allows three broad convection rolls that enhance circumferential melting. This geometric misalignment explains why the 4-fin case yields a lower average melting rate than the 3-fin case.

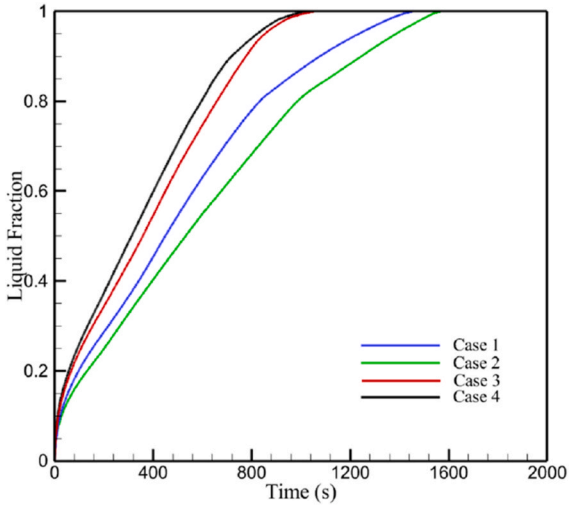

Fig. 8. Liquid fraction evolution vs. time for Cases 1–4 (effect of fin number; downward orientation).

The melting rate (W) represents the rate at which latent heat is absorbed by the PCM during phase transition. Physically, it quantifies how rapidly solid material is converted into liquid for a given thermal boundary condition. The melting rate is a direct indicator of the charging power of a LHTES unit. A higher melting rate signifies faster thermal response and greater heat uptake per unit time, which is essential for applications requiring rapid thermal buffering, load shifting, or high-power heat extraction. While the melting rate reflects instantaneous heat absorption, the liquid fraction describes the cumulative thermal energy stored. For LHTES systems, a faster rise in liquid fraction means quicker achievement of useable storage capacity. In the context of this study, comparing the liquid fraction evolution and melting rates of different configurations provides insight into how geometry influences global melting performance, charging duration, and the effectiveness of heat-transfer enhancements.

4.2. Effect of the fin dimensions

With the fin count fixed at six, two geometric variants were examined: increased fin length (Case 5) and increased fin thickness (Case 6). The liquid fraction fields in Fig. 12 are the primary evidence. At 300 s, Case 5 already shows circumferential connectivity of the melt along much of the inner perimeter, whereas Case 6 retains broad unmelted sectors centered between neighboring fins. By 600 s, Case 5 narrows these sectors further and the interface is nearly continuous around the tube; in Case 6, the interface remains segmented and noticeably recessed in the mid-gap regions. At 900 s, residual solid in Case 5 is confined to thin slivers near the outer shell, while Case 6 still exhibits appreciable un-melted regions between fins. These patterns indicate that extending fin reach preferentially assists circumferential transport into historically late-melting mid-gaps, while increasing thickness does not deliver comparable coverage.

The temperature fields in Fig. 13 explain the contrast. For Case 5, isotherms are denser near fin tips and more evenly distributed around the circumference, signalling stronger and more uniform heat penetration into the PCM. The longer fins create a shorter conductive path to mid-gap zones and simultaneously seed buoyant plumes that sweep along the perimeter; the result is a thinner, more continuous thermal boundary layer. In Case 6, thickening the fins elevates heat flux locally at the fin roots but leaves extended cool bands between fins and produces thicker near wall gradients, a signature of reduced lateral penetration. The additional solid volume also occupies space that would otherwise support convection, which helps to explain the slower late-stage advance of the melt front seen in Fig. 12.

Fig. 14 shows temperature fields at 300, 600, and 900 s for the six-fin variants with increased fin length (Case 5) and increased fin thickness (Case 6). In Case 5, closely spaced isotherms appear not only along the fin roots but also around the fin tips, and the high temperature region wraps more uniformly around the inner tube even at 300 s. By 600 s, the isotherms extend deeply into the inter-fin mid-gaps, indicating shorter effective conduction paths and stronger circumferential heat penetration. At 900 s, the thermal boundary layer remains comparatively thin and continuous along the perimeter, with only shallow cool sectors near the outer shell. In Case 6, the temperature field evolves differently. Isotherms cluster near the fin roots and decay rapidly across the mid-gaps at all times, leaving wide, cooler sectors between adjacent fins. The near wall thermal gradients are thicker, and the curvature of isotherms indicates weaker circumferential transport. The added fin mass increases local area and conduction at the roots but also occupies space where near wall recirculation would otherwise develop; the result is reduced lateral penetration and a slower equalization of wall temperature around the circumference. By 900 s, substantial cool bands persist between fins, explaining the delayed coalescence of the melt front in Fig. 12.

Taken together, the temperature contours in Fig. 14 show that extending fin length (Case 5) creates a more uniform and far-reaching thermal field, thin boundary layers, dense isotherms at the tips, and strong circumferential coverage, whereas increasing

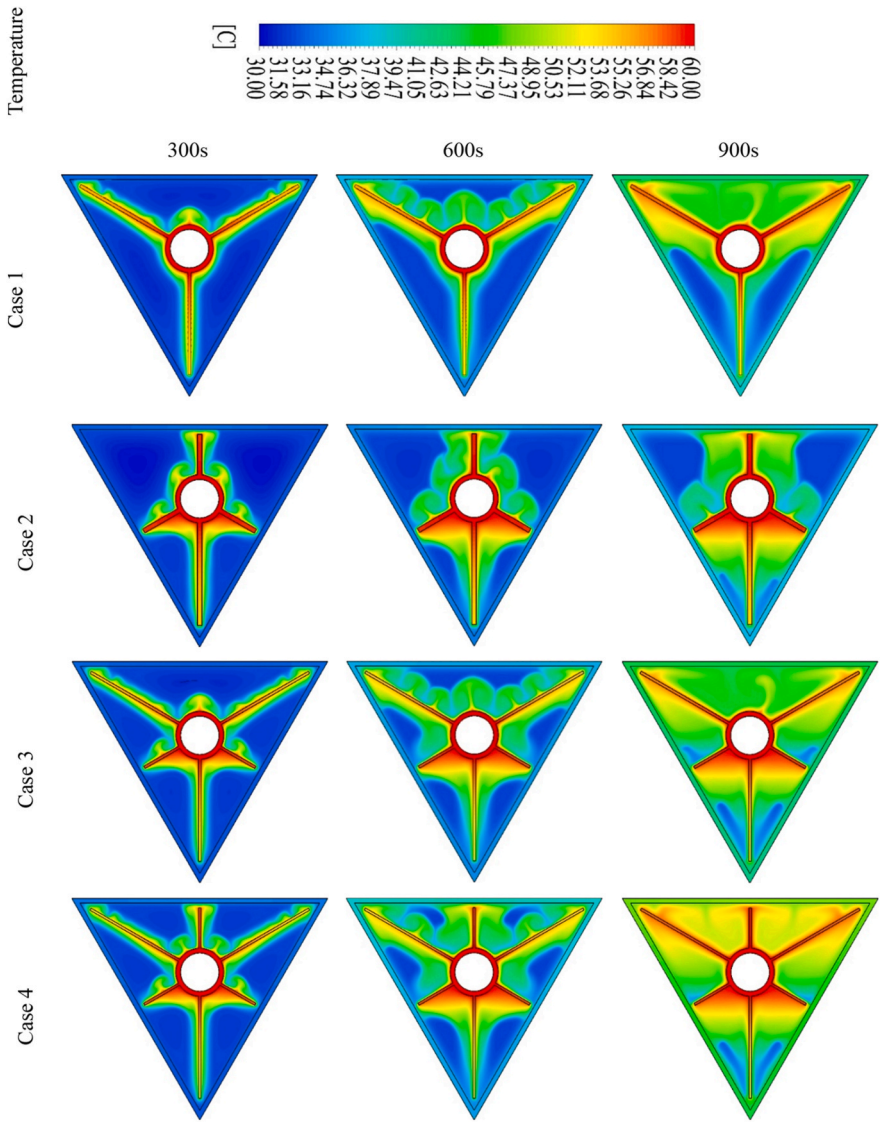

Fig. 9. Temperature distribution during the melting process for different fin configurations.

fin thickness (Case 6) concentrates heating near the roots and leaves mid-gap regions under-supplied.

Fig. 15 condenses the performance outcomes relative to the uniform six-fin baseline. Case 5 decreases the average melting (storage) rate by 11.8 % and increases melting time by 13.7 %, while Case 6 exhibits a larger penalty (24.1 % in rate, 33.1 % in time). Directly comparing the two variants, Case 6 operates at a 13.9 % lower rate and requires 17.0 % longer time than Case 5. Taken together, Figs. 12–15 show that, for six fins, extending fin length improves circumferential coverage and late-stage melting far more effectively than increasing fin thickness, which tends to concentrate heating near the roots and damp beneficial convection.

The difference between Case 5 (longer fins) and Case 6 (thicker fins) can be interpreted in terms of an effective heat-transfer resistance network. The total thermal pathway from the HTF tube to the bulk PCM consists of a series of conduction resistances (through the tube wall, fin, and nearby PCM) and a convection/transport resistance associated with buoyancy-driven circulation in the remaining liquid channels. Increasing fin thickness reduces the conduction resistance within the fin itself, but this benefit is offset by the displacement of PCM and the narrowing of flow passages, which increases the 'fluid-side' resistance and weakens recirculation, particularly in the mid-gap regions. Extending fin length, by contrast, primarily increases circumferential reach and contact area without constricting the flow channels to the same degree, so the convective pathway remains more effective. As a result, the net thermal resistance is lower for the longer-fin case than for the thicker fin case, which explains why the performance degradation is more pronounced in Case 6 than in Case 5.

The reduced performance of thicker fins can be explained by their altered thermal distribution. As shown in the temperature contours (Fig. 14), thicker fins exhibit stronger isotherm clustering near the fin roots, while the fin tips remain relatively cooler. This

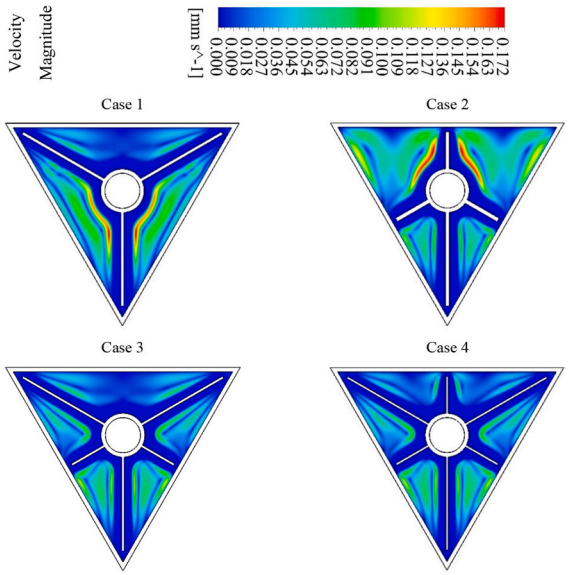

Fig. 10. Velocity-magnitude contours at t = 600 s for Cases 1–4, illustrating the effect of fin number on buoyancy-driven convection within the triangular enclosure. Regions of higher velocity (yellow–red) denote stronger recirculating cells and enhanced convective transport, while blue regions indicate weak flow.

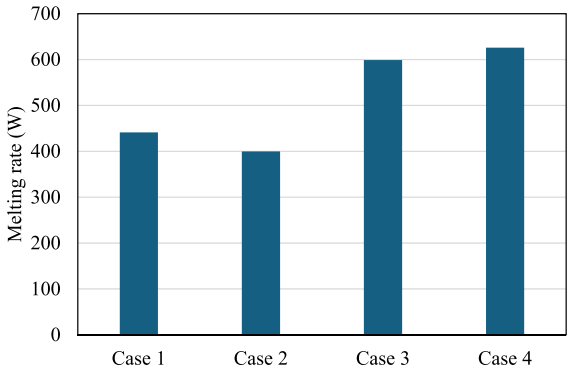

Fig. 11. Effect of fin number on average melting (heat storage) rate for Cases 1–4 in the downward orientation; the six-fin layout attains the highest rate.

indicates that axial conduction within the fin dominates over radial heat spreading toward the PCM. The resulting temperature gradients generate weaker buoyancy-driven plumes at the fin extremities, suppressing the circumferential convection loops responsible for rapid late-stage melting. This behavior is reflected in the performance metrics: thickening the fin (Case 6) lowers the average heat storage rate by 24.1 % and increases the melting time by 33.1 % relative to the baseline (Case 4). Thus, although thicker fins increase solid conduction paths, they simultaneously reduce the effectiveness of natural convection in the surrounding PCM.

4.3. Effect of angles between the fins for the downward shell (non-uniform fin distribution)

Fig. 16 shows that the non-uniform fin angles in Case 7 promote circumferential coalescence of the melt front at intermediate and late times. By 600 s the interface has bridged most inter-fin gaps, and by 900 s only thin residual sectors remain near the shell. This accelerated late-stage progression is consistent with Fig. 17: Case 7 completes melting earlier than the uniform six-fin baseline (4.7 % shorter time) while following it closely during the early and mid-stages. Fig. 16 indicates that the alternative angle set of Case 8 does not achieve comparable coverage. Wide unmelted regions persist between fins at 600 s and remain evident at 900 s, revealing weak lateral penetration. The corresponding LF–time curves confirm a slower progression throughout and a substantially delayed completion (24.7 % longer melting time relative to the uniform six-fin case), in line with the contour evidence.

Fig. 17 shows that all configurations follow similar early-stage growth, with the uniform six-fin baseline (Case 4) slightly ahead up to 500–600 s. Thereafter, the slope for Case 7 increases and the curve catches up, reaching the fully melted status marginally earlier than Case 4 (4.7 % shorter total melting time, consistent with the performance metrics), while Case 8 remains consistently lower and

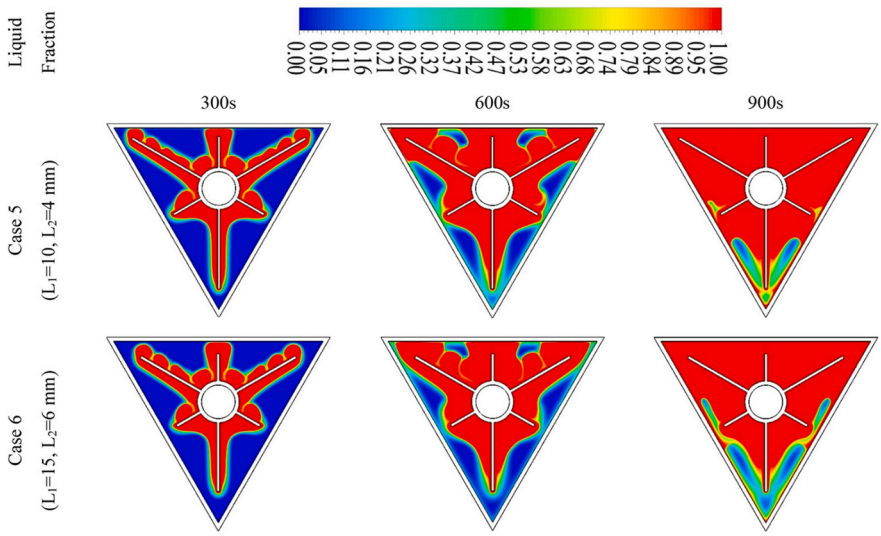

Fig. 12. Liquid fraction contours at 300, 600, and 900 s for six-fin dimensional variants.

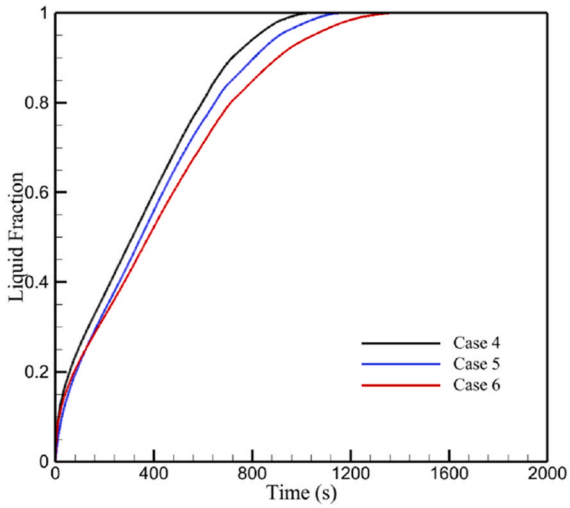

Fig. 13. Liquid fraction evolution for two cases 5 and 6 vs case 4 to show the effect of the dimension of fins.

attains full melting last (24.7 % longer than Case 4). This late-stage acceleration for Case 7 corroborates the liquid fraction contours in Fig. 16, where the interface coalesces circumferentially by 600–900 s, whereas the persistent deficit of Case 8 agrees with Fig. 16, which shows broad unmelted sectors between fins at comparable times.

The sustained melting rate observed for Case 7 in Fig. 17 can be understood from the interaction between fin layout and buoyancy-driven flow. In Case 7, the non-uniform angular distribution clusters several fins within the gravity-favoured sector, so that the buoyant plumes generated along these fins merge into a single robust circulation loop that persists throughout most of the charging period. This configuration continually brings fresh solid or partially melted PCM into contact with the heated fin surfaces, limiting the formation of stagnant cold pockets as the interface recedes. By contrast, the uniformly spaced six-fin case (Case 4) gradually develops stratified regions where convection weakens, leading to a more pronounced decay in melting rate at later times, and the unfavorable spacing in Case 8 leaves under-served circumferential sectors that further dampen circulation. As a result, Case 7 maintains a relatively high and weakly attenuated melting rate across the entire melting cycle.

Fig. 18 presents the temperature fields at 300, 600, and 900 s for the two non-uniform fin layouts. In Case 7, isotherms cluster at the fin roots and extend to the tips; by 600 s they form an almost continuous circumferential band around the inner tube, showing strong lateral heat penetration toward the inter fin mid-gaps. At 900 s, only shallow cool regions remain near the shell corners, and the near wall thermal layer is thin and uniform. In Case 8, the highest temperatures stay near the lower wedge and the fin roots, and spread less toward the spaces between fins, so larger cool areas are still visible even at 900 s. This clearer, more even heat spread in Case 7 explains its faster late-stage melting, while the limited spread in Case 8 explains its slower completion.

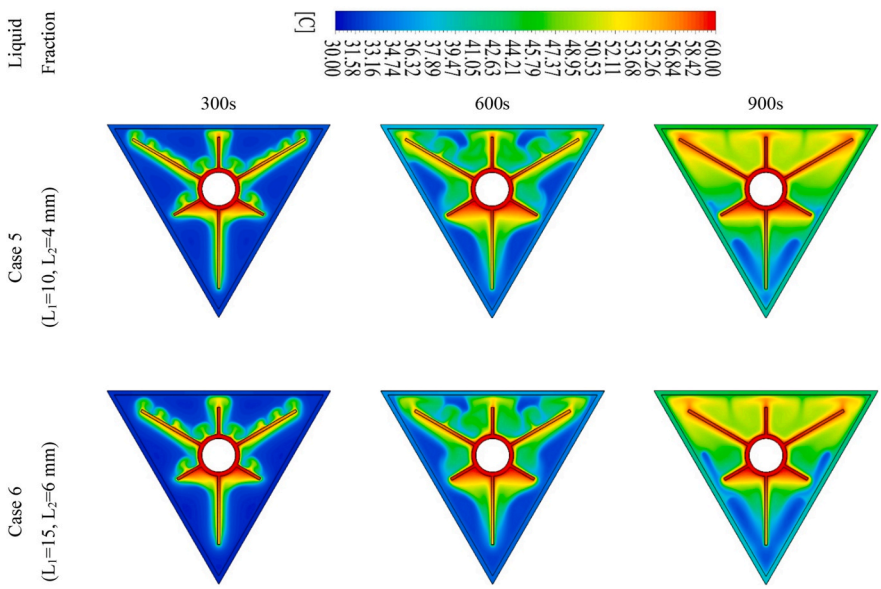

Fig. 14. Temperature contours at 300, 600, and 900 s for Cases 5 and 6.

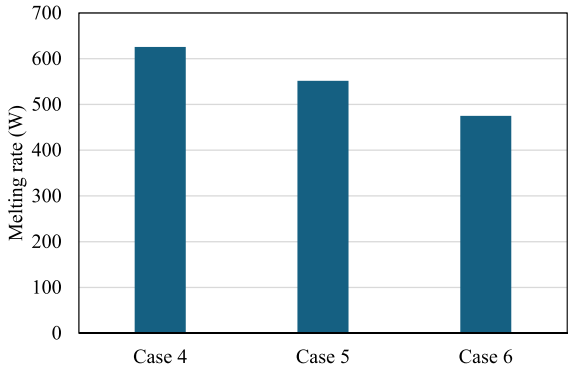

Fig. 15. Performance comparison for Cases 4–6: average melting rate.

The bar chart in Fig. 19 shows that the uniform six-fin baseline (Case 4) attains the highest average melting rate (626 W), while Case 7 is essentially comparable (619 W, only 1.1 % lower). Case 8 performs noticeably worse (497 W), representing a reduction of 20.6 % relative to Case 4 and 19.7 % relative to Case 7. These rate differences align with the field observations: Case 7's temperature contours exhibit broader circumferential heat spread and faster late-stage front coalescence (Fig. 18), whereas Case 8 retains cooler bands between fins and slower interface advance (Fig. 16).

Taken together, Figs. 15–18 demonstrate that the Case 7 angle set accelerates late-stage melting without materially increasing the average melting (storage) rate, whereas Case 8 degrades both rate and completion time. Because the study's selection criterion for the best downward configuration is the highest average melting rate, Case 4 remains the chosen design for subsequent comparisons, even though Case 7 finishes slightly sooner.

4.4. Effect of fin configurations on an upward shell

In Fig. 20, the three designs differ in both circumferential fin angles and radial reach. Case 9 concentrates the two upper fins toward the apex and extends their tips farther into the PCM; the side fins also have greater radial length than in the other variants. This geometry delivers heat directly into the top corners, where buoyant melt preferentially rises, so the LF contours show early bridging of the inter-fin gaps and rapid circumferential coalescence by 600–900 s. Case 10 relaxes that angular concentration and shortens the lateral reach, which leaves larger unmelted regions near the upper corners at the same time; LF grows more slowly and the interface remains segmented longer. Case 11 further reduces the effective coverage (wider angular spacing and shorter fin tips around the upper sector), producing the largest residual solid areas and the slowest front advance across the snapshots. The liquid fraction histories (Fig. 21) confirm these field observations: Case 9 reaches intermediate LF levels earlier and completes melting significantly sooner than

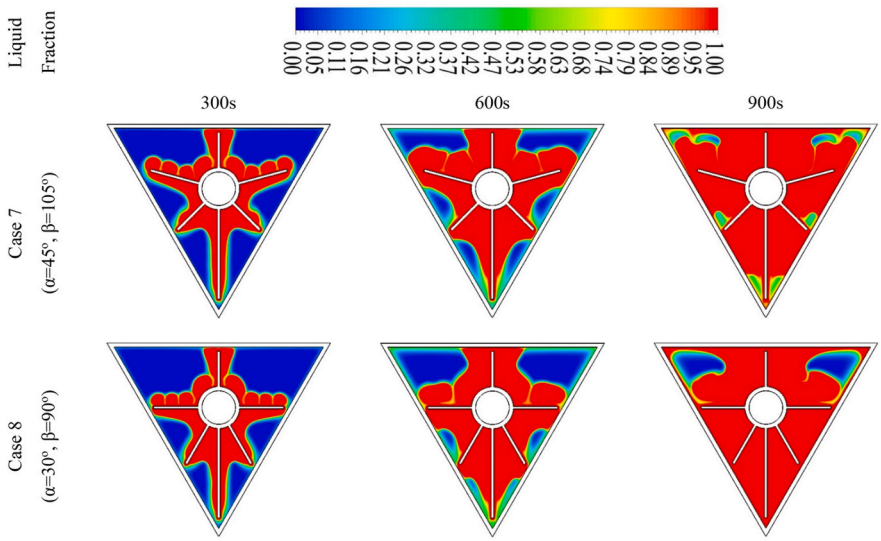

Fig. 16. Comparison of liquid fraction in two different configurations for the angle of fins.

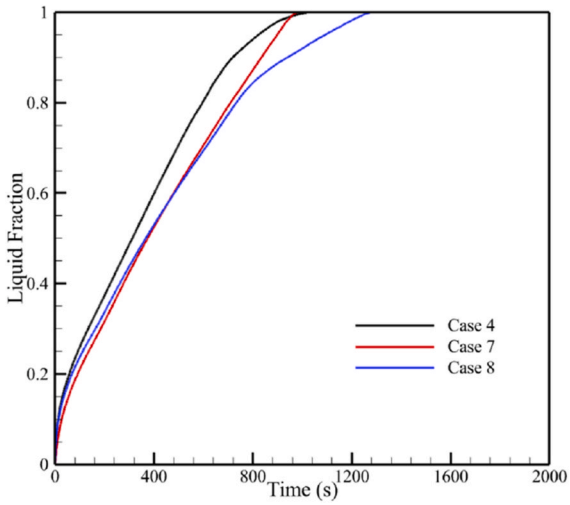

Fig. 17. Changing the liquid fraction in time for Case 7 (α = 45°, β = 105°) and Case 8 (α = 30°, β = 90°) vs case 4 (α = 60°, β = 120°).

Cases 10 and 11, consistent with the superior angular placement and longer fin lengths aimed at the upward sector.

The liquid fraction curves confirm the contour-based ranking. Case 9 attains intermediate melt levels earlier and reaches complete melting substantially sooner than Cases 10 and 11. Quantitatively, the total melting time for Case 9 is 956 s, compared with 1397 s (Case 10) and 1470 s (Case 11). Thus, Case 9 reduces charging time by 31.6 % versus Case 10 and by 35.0 % versus Case 11.

Three fin layouts are shown in Fig. 22, differing in both circumferential angle and radial length. In Case 9, the two upper fins are placed closer to the apex and extend farther into the PCM. This alignment with the buoyant up flow produces dense, continuous isotherms along the upper perimeter as early as 300–600 s, with the hot region reaching the top corners and spreading laterally between fins. By 900 s the near wall thermal layer is thin and uniformly wrapped, indicating efficient circumferential heat delivery. Case 10 relaxes the upper fin concentration and shortens the radial reach; isotherms remain less continuous around the apex, and cooler bands persist between the upper fins, showing reduced lateral penetration. Case 11 widens the upper angular spacing further and employs shorter fins; temperature maxima stay localized to the fin roots, with thick gradients and broad cool pockets in the upper sector even at 900 s. Overall, placing longer fins nearer the upward apex (Case 9) directs heat into the region where buoyant plumes accumulate, yielding the most uniform temperature field, whereas moving fins away from the apex and/or shortening them (Cases 10–11) limits thermal coverage and leaves under-heated zones that slow melting.

It has been shown in Fig. 23 that case 9 delivers the highest average melting (storage) rate at 667.2 W, compared with 464.5 W for Case 10 and 437.9 W for Case 11, gains of 43.6 % and 52.4 %, respectively. The corresponding melting times (956 s, 1397 s, and 1470 s) reflect the same hierarchy, matching the histories in Fig. 21 and the field patterns in Figs. 20 and 22.

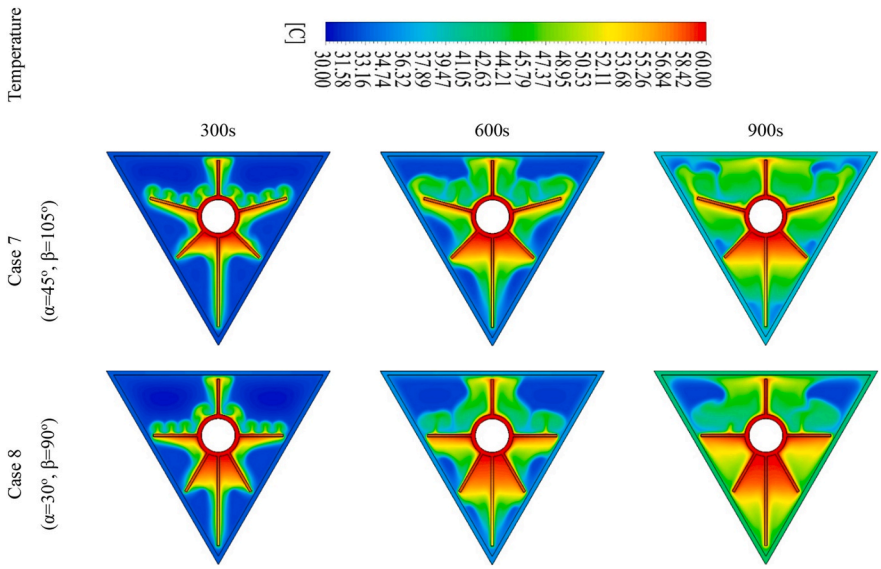

Fig. 18. Temperature distribution in non-uniform fin distribution.

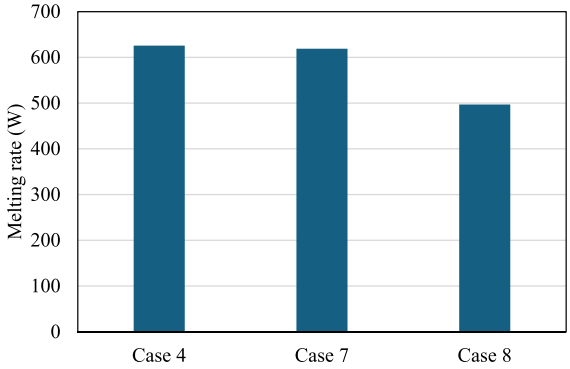

Fig. 19. Effect of fin angle on PCM melting rate.

The upward shell favors the Case 9 fin arrangement; it produces the most uniform circumferential heating, the fastest late-stage front coalescence, the shortest charging time, and the highest average storage rate among the tested variants. Accordingly, Case 9 is selected as the best configuration in the upward orientation for subsequent cross orientation comparisons.

4.5. Comparison of the best upward and downward cases

This section compares the optimal downward configuration (Case 4) with the optimal upward configuration (Case 9). Because both cases use identical fin geometry and material properties, the observed performance differences reflect the direct influence of gravity on natural convection development within the triangular enclosure. In the upward arrangement, buoyant flow rising toward the apex enhances recirculation and circumferential heat spreading, whereas in the downward arrangement, gravity suppresses plume development and weakens convective mixing. The comparison therefore isolates how orientation-dependent convection governs melting behavior under otherwise identical design conditions.

Fig. 24 shows the liquid-fraction contours at 300, 600, and 900 s for both configurations. In the Case 9, buoyancy forces drive the warm melted PCM toward the upper region of the enclosure, promoting earlier circumferential spreading and faster connection of the melt fronts between adjacent fins. By 600 s, the melt layer around the inner tube becomes more continuous, and by 900 s only small solid remnants remain near the bottom corners. In comparison, the downward orientation (Case 4) exhibits slightly slower circumferential progression: isolated solid pockets persist for longer between fins, and the melt front advances more gradually in the upper region of the cavity. Although both cases follow broadly similar melting patterns, the effect of gravity is clear, upward heating facilitates stronger recirculation near the top boundary, modestly enhancing melt uniformity.

These qualitative trends correspond well with the quantitative results in Fig. 25. Case 9 reaches complete melting in 956 s, compared with 1033 s for Case 4, representing a 7.5 % reduction in total melting time. The average heat-storage rate is also marginally

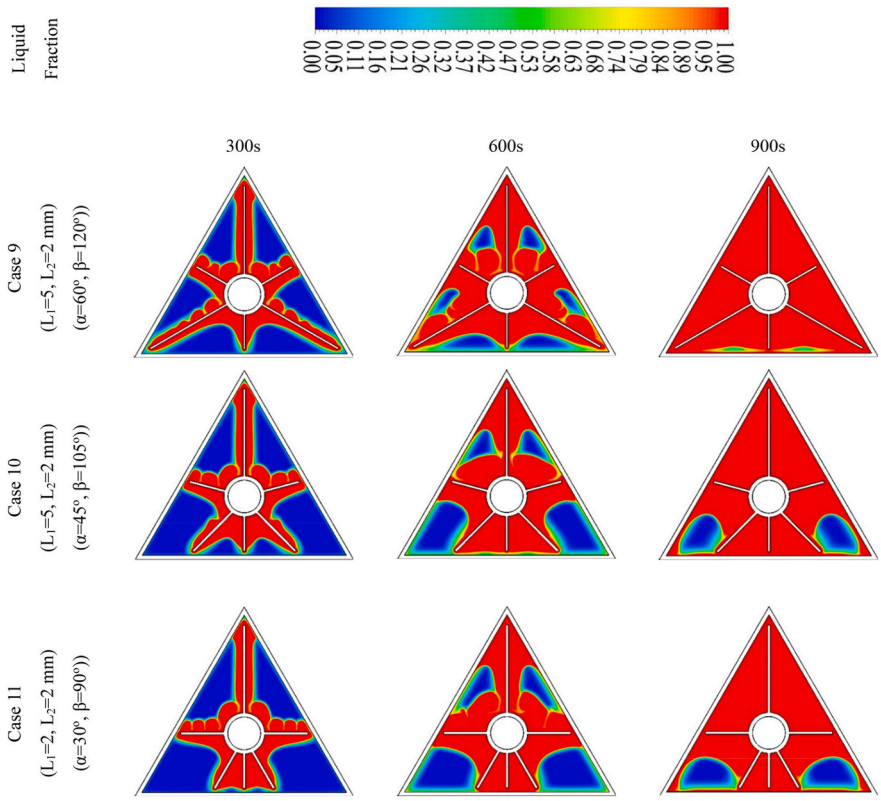

Fig. 20. Melting progress in upward shell for three different cases.

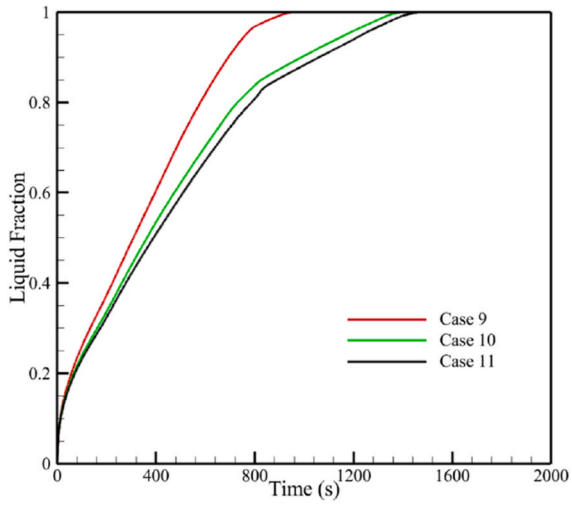

Fig. 21. Liquid fraction in upward shell for three different fin configurations.

higher for Case 9 (667 W) relative to Case 4 (626 W). The temperature evolution shows a similar trend: Case 9 experiences a slightly steeper rise in mean PCM temperature during the early and mid-stages of melting, consistent with the enhanced buoyancy-driven circulation present in the upward configuration.

Taken together, the results confirm that orientation introduces measurable but not drastic differences in melting performance for this triangular-shell LHTES unit. Because the upward configuration better aligns the buoyant plume with the fin layout and promotes more effective recirculation, Case 9 is identified as the superior overall design, achieving both a higher storage rate and a shorter total melting time under identical operating conditions.

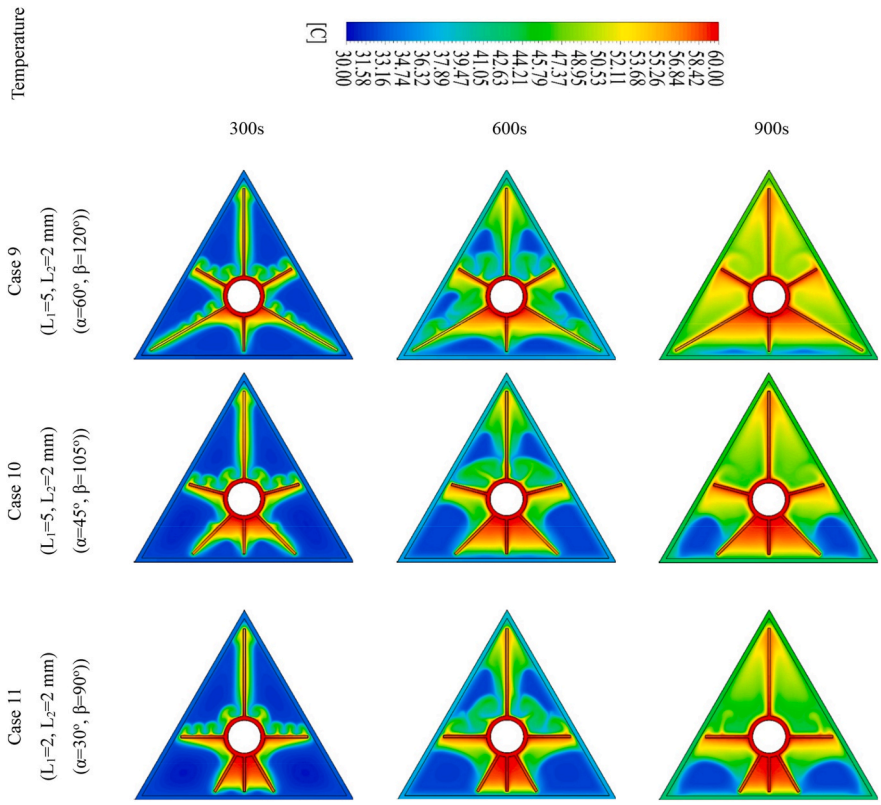

Fig. 22. Effect of the fin dimension and orientation on upward shell.

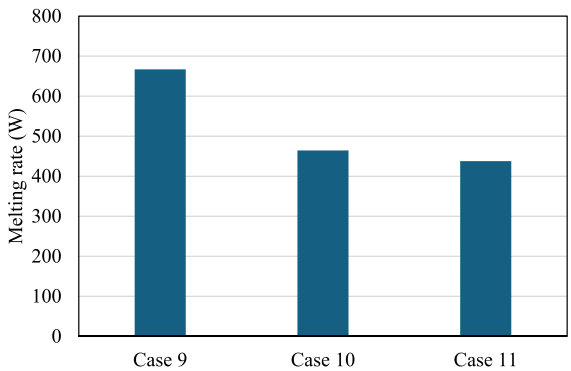

Fig. 23. Melting rate in upward shell for three cases.

In addition to the melting time and average/peak storage rate, we also examined scalar performance indicators commonly used in LHS evaluation, namely the total stored energy, the volumetric heat-storage density, and an energy-efficiency ratio impede convection. In the present study, all cases share the same PCM volume, thermophysical properties, and thermal boundary conditions (constant inner-wall temperature and adiabatic outer shell), and each configuration is charged until complete melting. As a result, the final PCM enthalpy increase—and thus and —is effectively identical for all fin layouts and both orientations. Under the same assumptions, the constant-temperature heating boundary supplies the same thermal driving potential, and the adiabatic shell ensures that essentially all of this input is stored in the PCM, so also takes the same value for every case. These integral indicators therefore cannot distinguish between the downward and upward configurations in the present framework. The metrics that meaningfully differentiate the designs are the charging rate and the melting completion time, which directly reflect how fin geometry and gravity alignment modify buoyancy-driven flow and the transient evolution of melting.

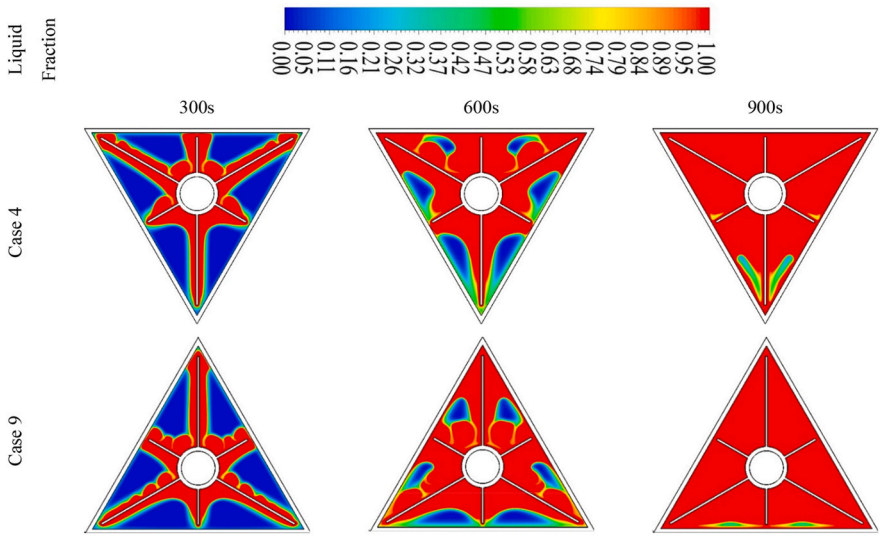

Fig. 24. Melting progress for case 9 and case 4 as the best in upward and downward orientation.

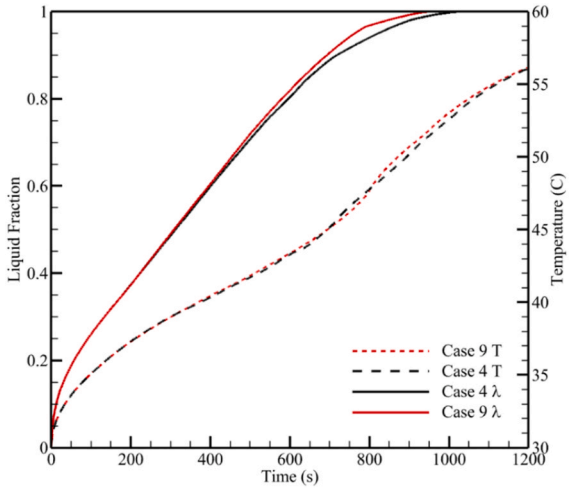

Fig. 25. Mean temperature and liquid fraction for the best upward and downward configurations.

5. Conclusion

This study analyzed a finned double pipe LHS unit within a triangular shell under downward and upward orientations, using identical material properties and a constant inner-wall temperature. The investigation proceeded by varying fin count (Cases 1–4), modifying fin dimensions on a six-fin baseline (Cases 5–6), and applying non-uniform circumferential fin spacing (Cases 7–8 downward; Cases 9–11 upward). The aim was to evaluate how fin number, geometry, placement, and orientation affect melting rate and completion time.

Increasing fins from three to six substantially improved performance, raising the average melting rate by 42 % and shortening melting time by 29.5 %. Five fins delivered most of the enhancement, while the four-fin arrangement performed worse than the three-fin baseline due to incomplete circumferential coverage. Adjusting fin dimensions demonstrated that added mass without improved reach can hinder melting: longer fins moderately reduced performance, and thicker fins imposed the largest penalties in both rate and time.

Non-uniform spacing revealed the importance of targeted circumferential access. Case 7 slightly reduced melting time relative to the uniform six-fin case, whereas Case 8 produced notable deterioration. For downward orientation, Case 7 is favorable for minimizing time, whereas Case 4 performs best under a rate-based metric.

Modifying fin dimensions showed that excessively thick or long fins reduce melting effectiveness. These configurations increase fin mass without proportionally improving circumferential heat spreading, resulting in lower overall melting rates.

Upward oriented designs consistently outperformed downward ones. Case 9 achieved the highest melting rate (667 W) and shortest melting time (956 s), benefiting from improved heating in the upper apex region. Compared with the best downward case (Case 4), the upward configuration increased melting rate by 6.5 % and reduced melting time by 7.5 %.

Overall, a six-fin architecture serves as a strong baseline, and indicates that the selected fin architecture effectively mitigates gravity-induced performance variation, reducing orientation sensitivity and improving applicability in installations where the unit may not be favorably aligned.

5.1. Key findings

- Increasing fin number from 3 to 6 enhances the average heat-storage rate by ~42 % and reduces melting time by ~29.5 %.
- Increasing fin length or thickness beyond the baseline six-fin design decreases performance due to suppressed natural convection.
- Non-uniform circumferential spacing improves melting performance for selected downward configurations but is less influential than fin number and orientation.
- Among the downward cases, Case 4 provided the best overall performance, striking a balance between conduction effectiveness and convective flow development.
- The upward optimal case (Case 9) outperformed the downward optimal case (Case 4) by only 6.5–7.5 %, illustrating that the chosen fin architecture substantially reduces orientation sensitivity and moderates the impact of gravity.

5.2. Limitations

The present study provides a detailed numerical evaluation of melting behavior in a finned double pipe LHS unit enclosed in a triangular shell; however, several limitations should be acknowledged. Only two gravitational orientations (vertical upward and downward) were examined, and intermediate inclination angles (e.g., 30–60°), which may produce distinct convection regimes, were not considered. A single PCM with fixed thermophysical properties was used, without assessing nano-enhanced or composite PCMs that could alter conduction and flow characteristics. Moreover, the analysis focused exclusively on the melting (charging) stage under a constant temperature boundary condition; discharge behavior and variable heat-input modes remain unexplored. Future work will extend the model to inclined orientations, advanced PCM materials, and discharge cycle to broaden the applicability of the findings.

CRediT authorship contribution statement

Fathi Alimi: Writing – review & editing, Writing – original draft, Methodology, Investigation, Data curation, Conceptualization. **Nashmi H. Alrasheedi:** Writing – review & editing, Writing – original draft, Supervision, Methodology, Funding acquisition, Conceptualization. **Mohammad Hossein Heidarshenas:** Writing – original draft, Visualization, Validation, Formal analysis. **Mohamed Bouzidi:** Writing – original draft, Supervision, Resources, Data curation, Conceptualization. **Mansour Mohamed:** Writing – review & editing, Writing – original draft, Visualization, Methodology, Investigation, Formal analysis. **Khalil Hajlaoui:** Writing – review & editing, Writing – original draft, Supervision, Funding acquisition, Data curation, Conceptualization. **Xusheng Hu:** Writing – review & editing, Writing – original draft, Methodology, Investigation. **Mehdi Ghalambaz:** Writing – review & editing, Writing – original draft, Validation, Project administration, Formal analysis, Conceptualization.

Funding statement

This work was supported and funded by the Deanship of Scientific Research at Imam Mohammad Ibn Saud Islamic University (IMSIU) (grant number IMSIU-DDRSP2503).

Declaration of competing interest

The authors clarify that there is no conflict of interest for report.

Data availability

Data will be made available on request.

References

[1] A.M. Soodmand, S. Nejatbakhsh, H. Pourpasha, H. Aghdasinia, S.Z. Heris, Simulation of melting and solidification process of polyethylene glycol 1500 as a PCM in rectangular, triangular, and cylindrical enclosures, Alex. Eng. J. 61 (11) (2022) 8431–8456.
[2] N.S. Dhaidan, Melting phase change of n-eicosane inside triangular cavity of two orientations, J. Renew. Sustain. Energy 9 (5) (2017).
[3] K. Fan, S. Zong, H. Gao, Z. Duan, Experimental study on thermal performance of PCM in an inclined shell-and-tube latent heat thermal energy storage unit, Processes 13 (5) (2025) 1557.
[4] M.A. Alnakeeb, W.M. Galal, M.E. Youssef, M.A.A. Salam, M.M. Sorour, Melting performance assessment of a latent thermal energy storage unit with multiple oriented elliptic tubes in various arrangements, J. Energy Storage 140 (2025) 119111.
[5] H.S. Sultan, M.H. Ali, J. Shafi, M. Fteiti, M. Baro, K. Almutairi, M.S. Islam, K. Harb, F.S. Alharbi, M. Ghalambaz, Design improvement of latent heat thermal energy storage in wavy channel enclosures using neural networks, J. Energy Storage 79 (2024) 110061.

[6] M. Ghalambaz, M. Aljaghtham, A.J. Chamkha, M. Fteiti, A. Abdullah, Latent heat thermal energy storage in a shell-tube: a wavy partial layer of metal foam over tubes, J. Energy Storage 59 (2023) 106493.
[7] N.B. Khedher, N. Biswas, H. Togun, H.I. Mohammed, J.M. Mahdi, R.K. Ibrahem, P. Talebizadehsardari, Geometry modification of a vertical shell-and-tube latent heat thermal energy storage system using a framed structure with different undulated shapes for the phase change material container during the melting process, J. Energy Storage 72 (2023) 108365.
[8] M.M. Zaytoun, M.M. El-Bashouty, M.M. Sorour, M.A. Alnakeeb, Heat transfer characteristics of PCM inside a modified design of shell and tube latent heat thermal energy storage unit, Case Stud. Therm. Eng. 49 (2023) 103372.
[9] H.A. Hasan, H. Togun, A.M. Abed, N.A. Qasem, A. Abderrahmane, K. Guedri, S.M. Eldin, Numerical investigation on cooling cylindrical lithium-ion-battery by using different types of nanofluids in an innovative cooling system, Case Stud. Therm. Eng. 49 (2023) 103097.
[10] A.H. Mathry, F.N. Al-Mousawi, N.S. Dhaidan, W.A. Al-Shohani, A.A. Alammar, Impact of design and operating parameters on the thermal performance of heat pipes: a review, J. Eng. Res. 13 (2) (2025) 985–1000.
[11] N.S. Dhaidan, F.N. Al-Mousawi, H.A. Al-Salami, R.Z. Homod, Melting of phase change materials in thermal storage unit with uniform and non-uniform distribution of fins, Sol. Energy 302 (2025) 114073.
[12] S.E. Ahmed, A. Abderrahmane, S. Alotaibi, O. Younis, R.A. Almasri, W.K. Hussam, Enhanced heat transfer for NePCM-melting-based thermal energy of finned heat pipe, Nanomaterials 12 (1) (2021) 129.
[13] Z. Haddad, D. Belkadi, A. Mourad, A. Aissa, Z. Said, O. Younis, A. Alazzam, E. Abu-Nada, Advancements and comprehensive overview of thermal management systems for lithium-ion batteries: nanofluids and phase change materials approaches, J. Power Sources 603 (2024) 234382.
[14] Z.A. Reheem, F.N. Al-Mousawi, N.S. Dhaidan, S.A. Kokz, Advances in heat pipe technologies for different thermal systems applications: a review: ZA Reheem et al, J. Therm. Anal. Calorim. 147 (23) (2022) 13011–13026.
[15] M. Zarei, S.M. Vahidhosseini, S. Rashidi, R. Rafee, W.-M. Yan, Review on the efficiency enhancement of solar-assisted heat pumps using nano-enhanced phase change materials (NEPCM), J. Energy Storage 114 (2025) 115804.
[16] Z. Liu, C. Li, Optimizing the geometric parameters of double branched fins for improving the melting performance of PCM, J. Energy Storage 118 (2025) 116284.
[17] N.S. Dhaidan, A.F. Hassan, A.M.R. Al-Gaheeshi, F.N. Al-Mousawi, R.Z. Homod, Experimental investigation of thermal characteristics of phase change material in finned heat exchangers, J. Energy Storage 71 (2023) 108162.
[18] F.L. Rashid, N.S. Dhaidan, A.J. Mahdi, S.A. Kadhim, K.A. Hammoodi, M.A. Al-Obaidi, H.I. Mohammed, S. Ahmad, S. Salahshour, E.B. Agyekum, Heat transfer enhancement of phase change materials using tree shaped fins: a comprehensive review, Int. Commun. Heat Mass Tran. 162 (2025) 108573.
[19] M. Ghalambaz, M. Shahabadi, S.M. Mehryan, M. Sheremet, O. Younis, P. Talebizadehsardari, W. Yaici, Latent heat thermal storage of nano-enhanced phase change material filled by copper foam with linear porosity variation in vertical direction, Energies 14 (5) (2021) 1508.
[20] M. Ghalambaz, H. Jin, A. Bagheri, O. Younis, D. Wen, Convective flow and heat transfer of nano-encapsulated phase change material (NEPCM) dispersions along a vertical surface, facta universitatis, series, Mech. Eng. 20 (3) (2022) 519–538.
[21] S. Sen, J.M. Mahdi, P. Talebizadehsardari, A. La Rocca, A. Cairns, Enhanced thermal management of lithium-ion pouch cells via hybrid approach of phase change material-liquid cooling, Int. Commun. Heat Mass Transf. 165 (2025) 108997.
[22] L.S. Raj, K. Yashwanth, C. Madan, A. Anusha, G. Sridarsi, S. Sreenivasulu, B.D. Prasad, Optimization study of radial finned latent heat storage system employing novel circumferential perforations, J. Energy Storage 79 (2024) 110068.
[23] P.D. Dhabarde, R.P. Soni, J.G. Suryawanshi, Passive-cooling of Li-ion batteries using PCM-metal foam in honeycomb enclosure, Appl. Therm. Eng. (2025) 128543.
[24] A. Belazreg, A. Abderrahmane, N.A. Qasem, N. Sene, S. Mohammed, O. Younis, K. Guedri, N. Nasajpour-Esfahani, D. Toghraie, Effect of Y-shaped fins on the performance of shell-and-tube thermal energy storage unit, Case Stud. Therm. Eng. 40 (2022) 102485.
[25] M. Benaissa, H.S.S. Aljibori, A.M. Abed, J.M. Mahdi, H.I. Mohammed, O. Younis, P. Talebizadehsardari, N.B. Khedher, Maximizing thermal response in latent heat thermal energy storage systems: a comprehensive study of wavy fin configuration and distribution, Int. Commun. Heat Mass Tran. 159 (2024) 108172.
[26] M. Boujelbene, J.M. Mahdi, A.M. Abed, M.S. Ghanim, K.A. Hammoodi, H.I. Mohammed, H. Togun, P. Talebizadehsardari, The potential of arch-shaped fins for energy-charge enhancement in triplex-tube heat storage: comparative analysis and optimization, J. Energy Storage 79 (2024) 110188.
[27] O. Younis, J. Shafi, S. Tiari, M. Ghalambaz, Artificial intelligence–numerical study of a 3D model of latent heat thermal energy storage with sine-shaped fins, J. Energy Storage 139 (2025) 118798.
[28] Y. Huang, C. Zhang, Y. Chen, Rapid charging and discharging strategies for latent heat storage, Renew. Sustain. Energy Rev. 222 (2025) 115953.
[29] N. Hu, Z.-R. Li, Z.-W. Xu, L.-W. Fan, Rapid charging for latent heat thermal energy storage: a state-of-the-art review of close-contact melting, Renew. Sustain. Energy Rev. 155 (2022) 111918.
[30] H.-R. Bahrami, O. Allahdadi, M. Ghaedi, Improving charging and discharging times in a latent heat storage using circumferential fins: a numerical study, J. Energy Storage 115 (2025) 115918.
[31] Z. Song, S. Wang, J. Hu, Y. Wang, X. Zhao, X. Yu, J. Guo, Analysis on the effect of heat transfer fluid tube shape on topology optimization fin configuration and heat transfer characteristics of latent heat thermal energy storage systems, International Communications in Heat and Mass Transfer 172 (2026) 110408.
[32] T. Xu, Integrating Latent Heat Storage into Residential Heating Systems: a Study from Material and Component Characterization to System Analysis, KTH Royal Institute of Technology, 2021.
[33] A. Klitou, T. Klitou, P.A. Fokaides, Modelling a packed-bed latent heat thermal energy storage unit and studying its performance using different paraffins, Int. J. Sustain. Energy 43 (1) (2024) 2306416.
[34] A.M. Rabi', J. Radulovic, J.M. Buick, Packed bed thermal energy storage system: parametric study, Thermoelectrics 4 (3) (2024).
[35] R. Andrzejczyk, T. Muszyński, M. Fabrykiewicz, M. Rogowski, Heat transfer enhancement of modular thermal energy storage unit for reversible heat pump cooperation, Int. J. Therm. Sci. 193 (2023) 108498.
[36] J. Wołoszyn, K. Szopa, Shell shape influence on latent heat thermal energy storage performance during melting and solidification, Energies 16 (23) (2023) 7822.
[37] J.T. Cieśliński, M. Fabrykiewicz, Thermal energy storage with PCMs in shell-and-tube units: a review, Energies 16 (2) (2023) 936.
[38] P. Talebizadeh Sardari, G.S. Walker, M. Gillott, D. Grant, D. Giddings, Numerical modelling of phase change material melting process embedded in porous media: effect of heat storage size, in: Proceedings of the Institution of Mechanical Engineers, Part A: Journal of Power and Energy, 2019 0957650919862974.
[39] J.M. Mahdi, E.C. Nsofor, Melting enhancement in triplex-tube latent heat energy storage system using nanoparticles-metal foam combination, Appl. Energy 191 (2017) 22–34.
[40] A. Shahsavar, A. Goodarzi, H.I. Mohammed, A. Shirneshan, P. Talebizadehsardari, Thermal performance evaluation of non-uniform fin array in a finned double-pipe latent heat storage system, Energy 193 (2020) 116800.
[41] A. Shahsavar, A. Shaham, P. Talebizadehsardari, Wavy channels triple-tube LHS unit with sinusoidal variable wavelength in charging/discharging mechanism, Int. Commun. Heat Mass Tran. 107 (2019) 93–105.
[42] P. Wang, X. Wang, Y. Huang, C. Li, Z. Peng, Y. Ding, Thermal energy charging behaviour of a heat exchange device with a zigzag plate configuration containing multi-phase-change-materials (m-PCMs), Appl. Energy 142 (2015) 328–336.
[43] M. Esapour, M. Hosseini, A. Ranjbar, Y. Pahamli, R. Bahrampoury, Phase change in multi-tube heat exchangers, Renew. Energy 85 (2016) 1017–1025.
[44] S. Mat, A.A. Al-Abidi, K. Sopian, M.Y. Sulaiman, A.T. Mohammad, Enhance heat transfer for PCM melting in triplex tube with internal–external fins, Energy Convers. Manag. 74 (2013) 223–236.
[45] W.-B. Ye, D.-S. Zhu, N. Wang, Numerical simulation on phase-change thermal storage/release in a plate-fin unit, Appl. Therm. Eng. 31 (17) (2011) 3871–3884.
[46] E. Assis, L. Katsman, G. Ziskind, R. Letan, Numerical and experimental study of melting in a spherical shell, Int. J. Heat Mass Tran. 50 (9) (2007) 1790–1804.

[47] A.A. Al-Abidi, S. Mat, K. Sopian, M.Y. Sulaiman, A.T. Mohammad, Internal and external fin heat transfer enhancement technique for latent heat thermal energy storage in triplex tube heat exchangers, Appl. Therm. Eng. 53 (1) (2013) 147–156.
[48] F. Agyenim, N. Hewitt, The development of a finned phase change material (PCM) storage system to take advantage of off-peak electricity tariff for improvement in cost of heat pump operation, Energy Build. 42 (9) (2010) 1552–1560.
[49] J.H. Nazzi Ehms, R. De Césaro Oliveski, L.A. Oliveira Rocha, C. Biserni, M. Garai, Fixed grid numerical models for solidification and melting of phase change materials (PCMs), Appl. Sci. 9 (20) (2019) 4334.